

Optimization and Analysis of 24/16/8 Hybrid Excitation Double Stator Bearingless Switched Reluctance Motor

Qianwen Xiang and Liyun Feng*

Abstract—In order to solve the strong coupling problem of a traditional bearingless switched reluctance motor (BSRM), this paper proposes a new type of hybrid excitation double stator BSRM (HEDSBSRM). The new motor can realize self-decoupling between torque and suspension force. In addition, the two degrees of freedom suspension force can also be decoupled. First, the topology of the motor is proposed, and the generation mechanism of suspension force and torque are expounded. Second, the torque winding structure is optimized. The multi-objective sensitivity optimization design method is used to screen out the key structural parameters that have the greatest influence on the average suspension force, average torque, and core loss. Then, the optimal structural parameters are obtained by the control variable method. Finally, based on the optimized motor, the finite element method (FEM) is used to analyze the electromagnetic characteristics including the suspension force, torque, and coupling of the motor. The simulation results verify the correctness of the proposed design method and analysis of motor performance.

1. INTRODUCTION

Owing to simple structure and high efficiency, switched reluctance motor is suitable for a lot of industrial applications. Due to low critical speed and increased frictional resistance, traditional mechanical bearing limits further increase of the critical speed of motor [1–4]. The emergence of magnetic bearing technology overcomes the shortcomings of mechanical bearing [5–10]. However, magnetic bearing increases the axial length of the motor and limits further increase of critical speed of the motor. BSRM combines the advantages of magnetic bearings and switched reluctance motors, such as no mechanical wear, no lubrication, and high critical speed.

Some researches of BSRM in optimization design, mathematical modeling, control strategy, and non-displacement sensor control have been studied [11–21]. It is found that the coupling problem of BSRM seriously affects the running performance and popularity of the motor, which restricts the development of engineering applications. In order to solve this problem, nonlinear decoupling control of neural network inverse and support vector machine inverse are proposed in [11–13]. However, the inverse model algorithm is complex and difficult to be used in engineer applications. Moreover, the inverse model adopts the method of off-line modeling and on-line detection, which is difficult to adapt to the requirements of the time-variation of the motor under high-speed operation. Therefore, some novel BSRM topologies with self-decoupling functions have been proposed [14–17].

In [14, 15], a novel BSRM with biased permanent magnets (PM) is presented. It consists of two motors, and each motor has two radial control degrees of freedom. When the rotor center is eccentric, suspending force is generated by the control flux from the suspending force pole and biased flux from the PM. The structure has a certain size requirement for the axial length of the PM and two motor shafts. If the axial length of the PM or the shaft is too short, the bias magnetic flux cannot completely

Received 21 November 2018, Accepted 14 December 2018, Scheduled 4 January 2019

* Corresponding author: Liyun Feng (fly_95@163.com).

The authors are with the School of Electrical and Information Engineering, Jiangsu University, Zhenjiang, Jiangsu 212013, China.

pass through the front and rear motors, and it will affect the electromagnetic performance. Therefore, the axial length of this motor is too long, and the motor structure is complicated, leading to a difficult assembly process and high control cost. In [16], a novel 12/14 bearingless permanent magnet biased SRM is introduced. In order to prevent the PM from short-circuiting and provide a path for controlling the magnetic flux, a secondary air gap is designed in the stator. However, due to the limited width of the secondary air gap, there still exist some short circuits of the PM and magnetic leakage. The control flux generated by the suspension winding can pass through the PM to generate the risk of demagnetization with the increase of the secondary air gap width. In [17], a double stator BSRM (DSBSRM) is proposed by Wei et al. The winding on the outer-stator of the motor provides the torque, and the winding on the inner-stator provides the suspension force. Since the size of inner-stator is small, and it is excited by the electric excitation method, the suspension force is limited, and the power is small. Besides, the suspension windings on the four poles of the inner-stator are independently controlled and separately excited, resulting in a large number of switching devices and high cost.

This paper is devoted to the analysis of HEDSBSRM and electromagnetic characteristics of the motor. In this paper, Section 2 introduces the structure and working principle of the motor in detail. In Section 3, torque winding is analyzed and optimized. Then the motor is optimized in order to increase the average suspension force and average torque, and reduce the iron loss. The multi-objective optimization design method based on “parameter sensitivity analysis” is used to obtain key structural parameters that have the greatest impact on the optimization objectives. The electromagnetic properties are verified by finite element analysis in Section 4. The results show that the multi-objective optimization design method is suitable for the optimization design of HEDSBSRM. The methods proposed in this paper also have reference values for other complex bearingless motors.

2. TOPOLOGY AND PRINCIPLE

2.1. Topology of Proposed Motor

The topology of the novel HEDSBSBM is shown in Fig. 1. The material of core is silicon steel sheet DW465-50, and that of the PM is NdFe30. The motor consists of a 24-pole outer-stator, a 16-pole rotor and an 8-pole hybrid inner-stator. They are coaxially nested from inside to outside in order. Eight poles of inner-stator and PM are both secondary symmetrically distributed. The radial width of PM is equal to the width of outer-stator poles to prevent leakage of the PM. The PM is radially magnetized to provide bias magnetic flux. The 8-pole magnetic field is formed by the control and bias magnetic flux simultaneously. The magnetic poles change alternately with NS. The blue arrow in the figure shows the direction of radial magnetization of the PM. The suspension current in the x -direction controls the

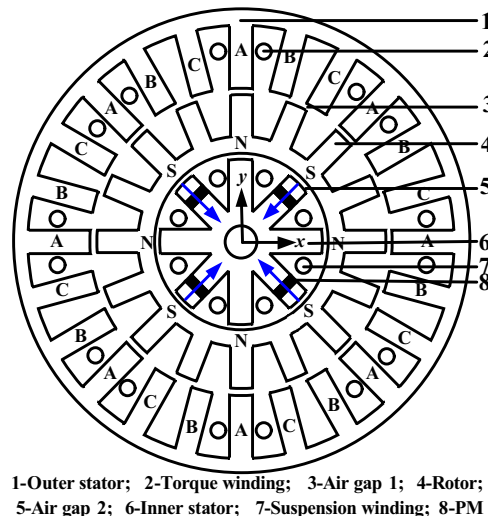


Figure 1. Topology of HEDSBSRM.

suspension force in the x -direction. The suspension current in the y -direction controls the suspension force in the y -direction. The 24 poles of outer-stator are uniformly distributed. The windings on 8 poles are connected in series to form one phase, as shown in phase A of the figure. Phases B and C are respectively located at 15° and 30° in the clockwise direction of phase A.

2.2. Principle of Proposed Motor

In Fig. 2(a), for the proposed motor, the working principle of the torque is similar to the conventional SRMs which follow the “minimum principle of reluctance”. When phase A is excited, a closed magnetic circuit is formed through the outer-stator, air gap 1, and rotor. Distortion of magnetic field produces tangential force, which is used to drive the rotor to rotate.

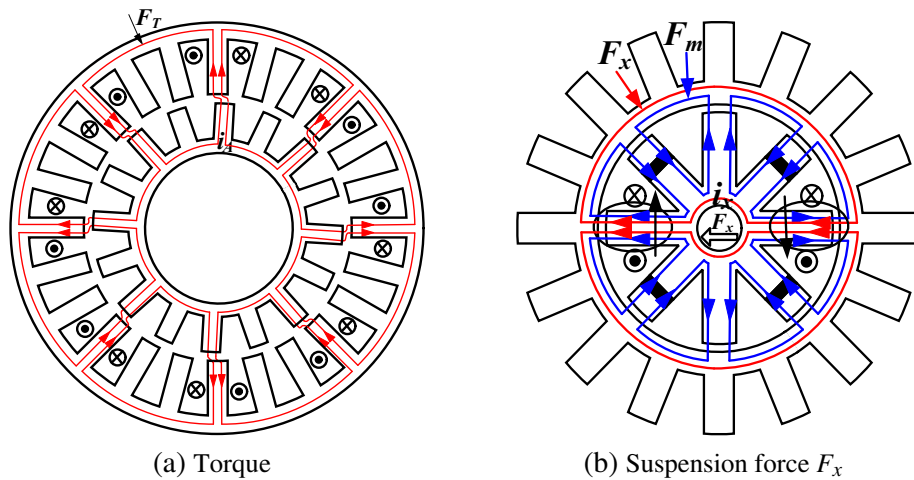


Figure 2. Operating principle of HEDSBSRM.

As shown in Fig. 2(b), the suspension force of the motor is generated by the PM in the inner-stator and suspension winding. The bias magnetic flux provided by the PM (shown by the blue line in the figure) is closed through the magnetic pole with the PM, air gap 2, rotor yoke, air gap 2, control magnetic pole, and stator yoke. The magnetic flux generated by the suspension windings (shown by the red line in the figure) is closed through the control magnetic pole, air gap 2, rotor yoke, air gap 2, control magnetic pole, and stator yoke. Due to the large magnetic resistance of the PM, the control magnetic circuit does not pass through the pole with the PM. Therefore, the PM is not demagnetized, and there is no short circuit.

The current of torque is taken as i_A , and i_x and i_y are the current of suspensions in x -direction and y -direction, respectively. Taking suspension force in the x -direction as an example, when $i_x = 0$ A, due to the symmetry of the magnetic circuit, the bias magnetic density at air gap 2 is equal under the action of the PM. In this case, $F_x = 0$ N, and the rotor is in the equilibrium position. When the rotor is disturbed and shifted to the positive x -direction, the magnetic field is unbalanced in the left and right directions of the x -direction. Then, air gap 2 in the positive x -direction and the magnetic field become smaller. And the air gap 2 in the negative x -direction and the magnetic field become larger. At this time, control the suspension current in the x -direction, and it will generate the control flux in the negative x -direction. The control magnetic field is superimposed on the bias magnetic field in the negative x -direction. Air gap 2 is reduced, and the magnetic field is increased in the negative x -direction. The magnetic flux generated by the bias magnetic field in the positive x -direction is weaker than the opposite side. Then, a pulling force in the negative x -direction is generated, and the rotor will be pulled back to the equilibrium position.

3. DESIGN AND OPTIMIZATION

3.1. Selection of Torque Windings

The outer-stator with 24 poles is divided into three phases. The windings of each phase have the following four excitation modes according to different current excitation modes (such as phase A): mode 1: NSNSNSNS, mode 2: NSSNNSN, mode 3: SNSNSNSN, and mode 4: NNNNNNNN. When $i_A = 4\text{ A}$ and $i_x = i_y = 0\text{ A}$, the magnetic flux of the control magnetic field and the bias magnetic field of the PM are shown in Fig. 3.

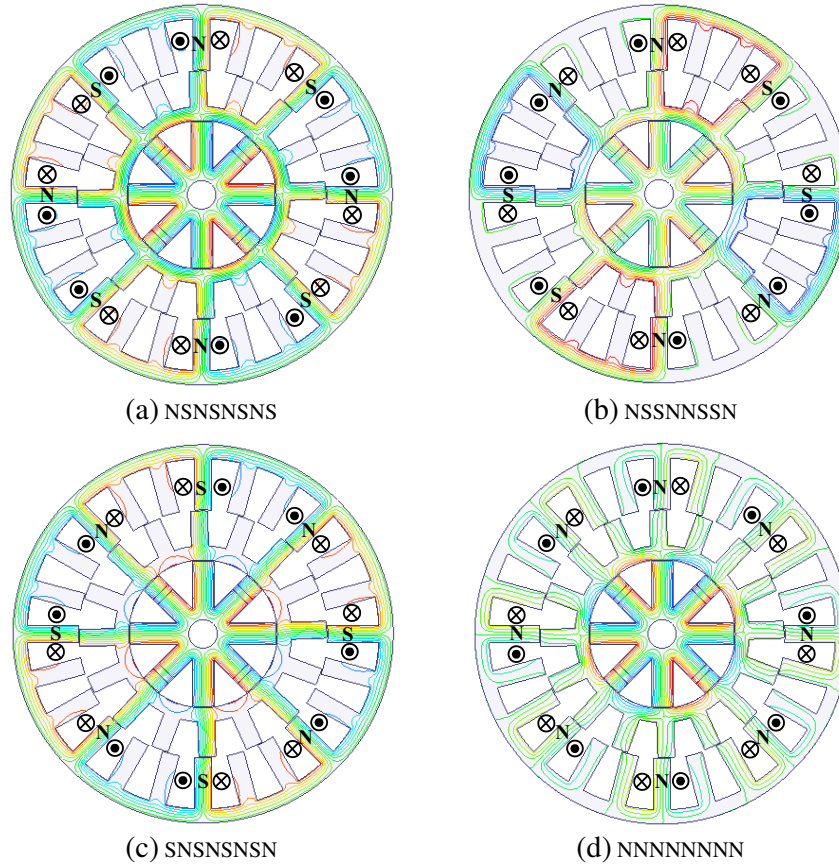


Figure 3. Different excitation modes of torque windings.

In Fig. 3(d), it can be seen that the magnetic flux at air gap 1 in mode 4 is the least, which causes the smallest torque during the four methods, thus, method 4 is not feasible. The torque magnetic circuit is short of mode 1, partial long and partial short of mode 2, and long of mode 3. These three types of excitation methods have the same magnetic flux at air gap 1. Therefore, the torques generated by these three modes are basically the same. In addition, the distributions of magnetic flux in the outer-stator and rotor are different in mode 1/2/3. In mode 2/3, the bias magnetic circuit of the PM and the magnetic circuit of torque are coupled to each other. Besides, the magnetic circuit of torque generated by the electric excitation passes through the PM on the inner-stator, which increases the risk of demagnetization and affects the stable operation of the motor. Therefore, mode 1 is selected as the connection method of the torque windings. It can realize the independence of the suspension magnetic circuit and rotating magnetic circuit. Besides, due to the action of the short magnetic circuit, the core loss is reduced.

3.2. Initial Design

3.2.1. Design Ideas

The external of the HEDSBSRM motor follows the basic design idea of the ordinary SRM motor, and the interior follows the basic design idea of the magnetic bearing. The basic dimensions of the motor are determined according to the principles from inside to outside. Fig. 4 shows the basic design flow of the motor.

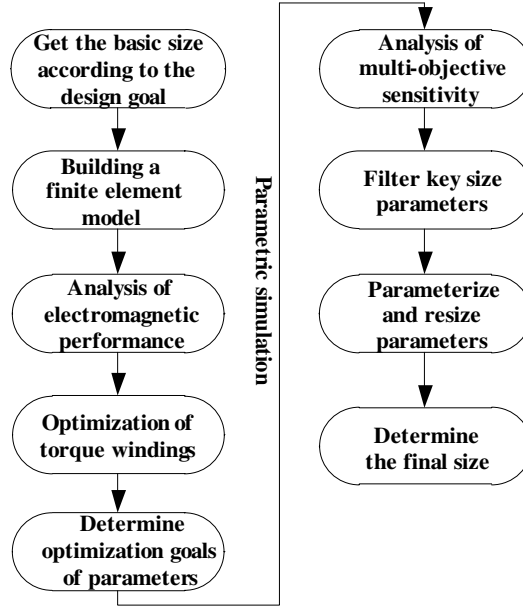


Figure 4. Design flow.

Due to the consideration of the basic design requirements of BSRM, the initial size is determined based on the design experience of SRM and magnetic bearing. Then, a motor model is built by using Maxwell (a finite element analysis software). Its electromagnetic properties are analyzed through simulation. Meanwhile, optimization goals are established. On the basis of the analysis of multi-objective sensitivity, the critical dimensions are selected, and the parameters are optimized and adjusted to obtain the results of final size.

3.2.2. Equation of Basic Size

The main structural dimensions of HEDSBSRM are rotor outer diameter, magnetic pole area of inner-stator, and axial length. Based on empirical formulas (1)–(3) of SRM and magnetic bearing, the principle of internal to external is used to determine the motor, which can be expressed as

$$D_{ro} = \sqrt[3]{\frac{6.1 \cdot k_i P_{em}}{B_\delta A k_m n \cdot 1.05 \lambda}} \quad (1)$$

$$F_{xy} = \frac{2n_p B_{xyb} B_{xyc} S_{xy} \sin\left(\frac{f_i \cdot \pi}{n_p}\right)}{\pi \cdot \mu_0 f_i} \quad (2)$$

where D_{ro} is the outer diameter of rotor; P_{em} is the electromagnetic power; B_δ represents the magnetic loading, and the value range is 0.3 T ~ 0.6 T; A represents the electric loading, and the value range is 15000 ~ 50000 A/m; n represents the rated speed; λ is the slender ratio, ranging from 0.5 to 3; f_i is the inner-stator duty ratio; magnetic density of air gap 2 is taken as 1.3 T; B_{xyb} and B_{xyc} are biased and control magnetic density, respectively; F_{xy} is the suspension force; S_{xy} is the magnetic pole area

of inner-stator; n_p is the number of inner-stator poles. In order to maximize the bearing capacity, the values of B_{xyb} and B_{xyc} are equal.

The design goals of HEDSBSRM are that the rated power is 1.8 kW, and the rated speed is 7000 rpm. The air gap length is selected as 0.3 mm. Since the rotor yoke thickness is limited and is easy to saturate, the suspension force is set as 150 N. Under the consideration of the practicality of the current conduction interval and mathematical model, the pole arcs of the rotor and outer-stator are equal. Thus, the initial motor size can be determined as shown in Table 1.

Table 1. Initial size of the major parameters.

| Parameters | Value |
|--|-------|
| Inner-stator Pole Area/mm ² | 255 |
| Outer-stator Outer Diameter/mm | 113 |
| Rotor Outer Diameter/mm | 72 |
| Outer-stator Inner Diameter/mm | 72.3 |
| Inner-stator Width | 6 |
| Rotor Yoke Thickness/mm | 3.3 |
| Outer-stator Yoke Thickness/mm | 4.2 |
| Rotor Depth/mm | 10.3 |
| The rotor pole arc | 7 |
| Axial Length/mm | 37.5 |
| PM Length/mm | 2.2 |

Based on the above analysis, the proposed motor is parametrically modeled in Maxwell 2D to adjust the parameters in subsequent optimizations.

3.3. Optimization and Adjustment

3.3.1. Determination of Optimization Goals

The average suspension force, average torque and core loss are selected as the main optimization objectives. The target is to reduce the core loss and increase the average suspension force and torque at the same time.

The average suspension force F_{avg} is calculated as

$$F_{avg} = \frac{F_1 + F_2 + \dots + F_n}{n} \quad (3)$$

wherein the rotor rotation angle is in the range of $[0, 7.5^\circ]$; n is the number of angle sampling points which is taken as 10; and F_n is the corresponding suspension force value of each sampling point.

Similarly, the corresponding torque and core loss of each sampling point are recorded as T_n and P_n , and the average torques T_{avg} and P_{avg} are calculated as

$$T_{avg} = \frac{T_1 + T_2 + \dots + T_n}{n} \quad (4)$$

$$P_{avg} = \frac{P_1 + P_2 + \dots + P_n}{n} \quad (5)$$

3.3.2. Analysis of Parameter Sensitivity

According to the initial size and design requirements of SRM in Table 1, seven structural parameters are selected for analysis of multi-objective sensitivity. The motor was simulated by Maxwell, and its optimization range is listed in Table 2 below.

Table 2. Range of parameter optimization.

| Parameters | Value |
|--|-------------------------|
| Rotor Width b_r /mm | 3.77 ~ 6.28 |
| Outer-stator Width b_{is} /mm | 3.8 ~ 6.33 |
| Rotor Yoke Thickness h_r /mm | 2.64 ~ 4.4 |
| Outer-stator Yoke Thickness h_{is} /mm | 2.66 ~ 4.43 |
| The rotor pole arc β | $6^\circ \sim 10^\circ$ |
| Rotor Depth d_r /mm | 10.1 ~ 11.86 |
| PM Length l_p /mm | 1.2 ~ 2.6 |

The multi-objective sensitivity analysis method is used to screen out the parameters that have a great influence on the optimization target, and the results are shown as follows.

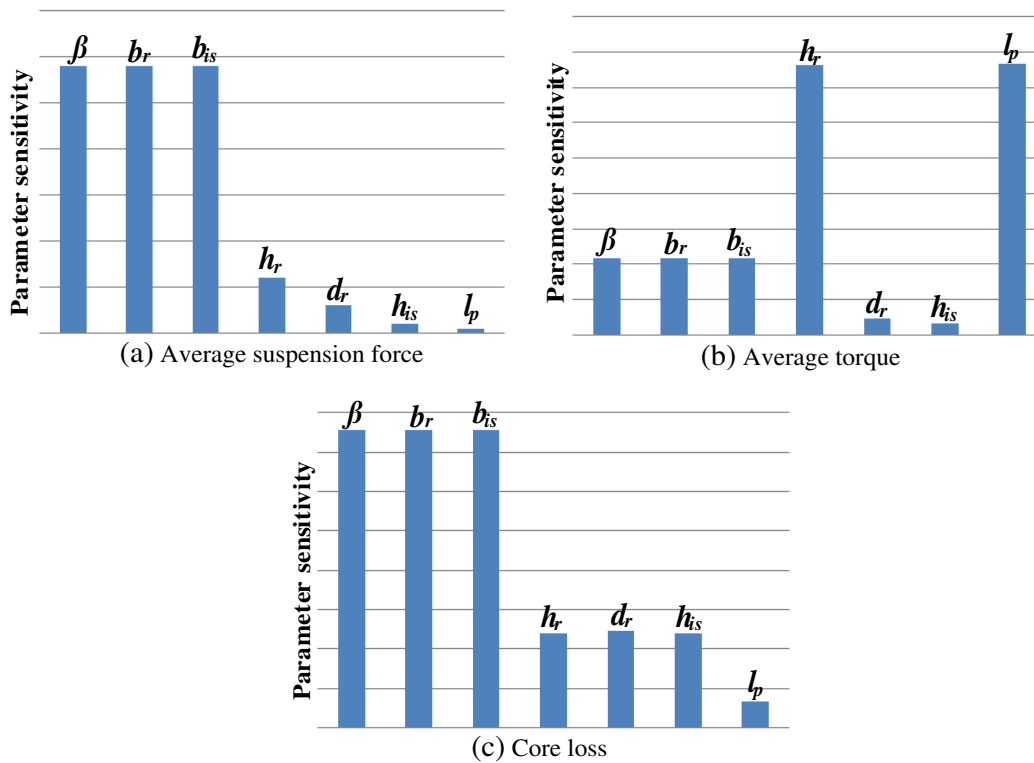


Figure 5. Sensitivity of HEDSBSRM.

In Fig. 5, it can be seen that rotor yoke thickness and PM length have a greater influence on the average torque while the rotor pole arc and width of rotor and outer-stator have a greater impact on average suspension force and core loss. The width is proportional to pole arc. Therefore, the pole arc, rotor yoke thickness, and PM length are selected for parameter optimization.

3.3.3. Optimization and Adjustment of Parameters

For the three optimization objectives in Section 3.3.1, the selected parameters are optimized by the control variable method. When the torque winding is excited in one phase and $i_A = 4\text{ A}$, $i_x = 2\text{ A}$, three optimization objectives vary with the three optimization objectives, as shown in Figs. 6, 7 and 8,

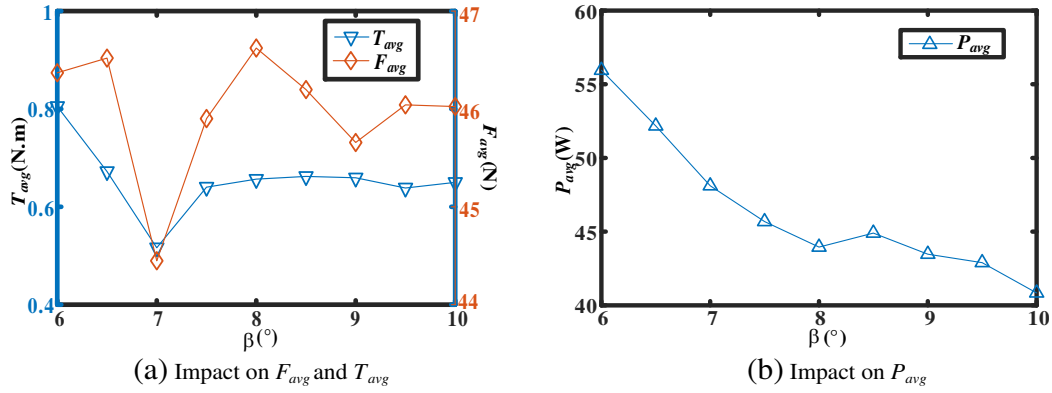


Figure 6. Optimization of outer-stator and rotor pole arc.

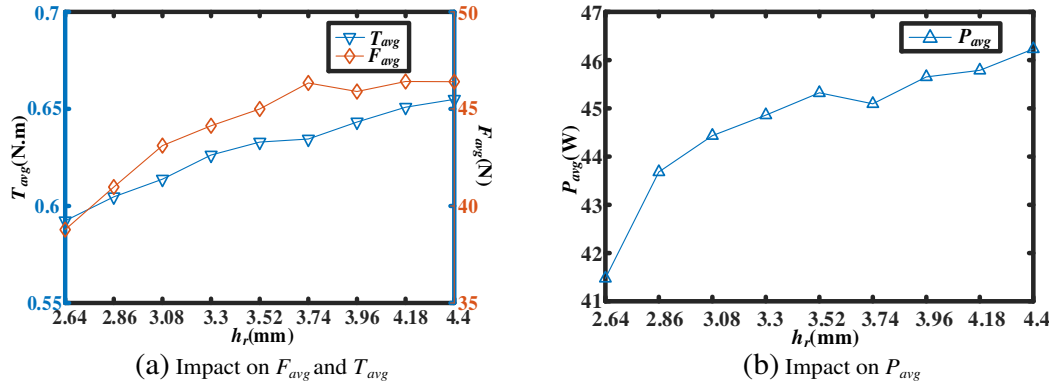


Figure 7. Optimization of rotor yoke thickness.

respectively. The optimization objectives also reflect the variation of magnetic density from different angles. Fig. 6 shows the relationship between the rotor pole arc and optimization target. In Fig. 6(a), as the pole arc increases, the average torque decreases at first, then increases and finally tends to be gentle. The average suspension force changes up and down. The pole arc is suitable within the range of 7.5° to 8.5° . In Fig. 6(b), the core loss decreases linearly. After considering comprehensively, the rotor pole arc is taken as 8° .

Figure 7 shows the relationship between the rotor yoke thickness and optimization objectives. In Fig. 7(a), as the rotor yoke thickness increases, the average torque and average suspension force both increase linearly. In Fig. 7(b), the core loss increases with the enlargement of the rotor yoke thickness. Thus, the rotor yoke thickness is taken as 4.18 mm at last.

Figure 8 shows the relationship between the PM length and optimization objectives. In Fig. 8(a), as the PM length increases, the average torque decreases linearly, and average suspension increases linearly. In Fig. 8(b), the core loss increases linearly. Finally, the PM length is taken as 2 mm after comprehensive consideration.

The optimization results of the main parameters of the motor are shown in Table 3 below.

In order to verify the influence of parameter optimization on the objective function, the initial size and adjusted parameters are simulated separately. The analysis and comparison results are shown in Table 4.

In Table 4, it can be found that, after optimization, the average suspension force and average torque have been improved, and the core loss has been decreased. Thus, it can be concluded that the motor performance has been further improved after optimization.

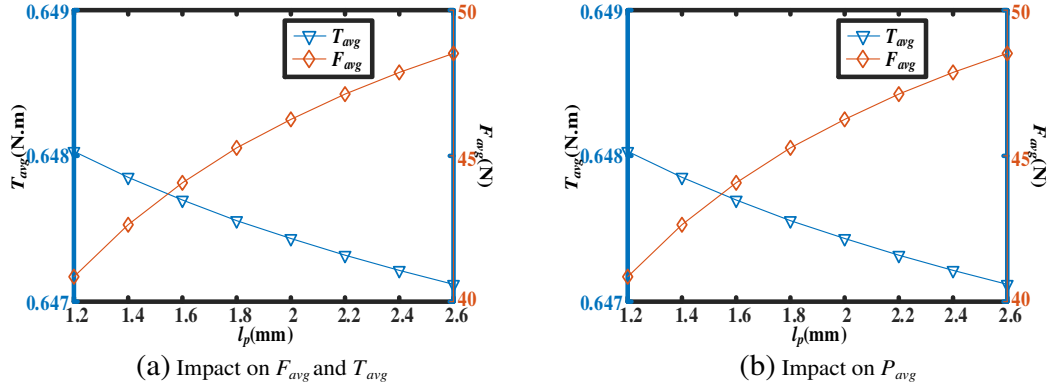


Figure 8. Optimization of PM length.

Table 3. Result of parameter optimization.

| Parameters | Value |
|-------------------------|-------|
| Rotor pole arc | 8° |
| Rotor Width/mm | 5 |
| Outer-stator Width/mm | 5.1 |
| Rotor Yoke Thickness/mm | 4.18 |
| PM length/mm | 2 |

Table 4. The impact of optimization on performance.

| Optimized target | Initial size | Final size |
|------------------|--------------|------------|
| F_{avg}/N | 45.8 | 46.3 |
| T_{avg}/N | 0.58 | 0.67 |
| P_{avg}/W | 44.2 | 42.8 |

4. ANALYSIS OF ELECTROMAGNETIC CHARACTERISTICS

4.1. Finite Element Analysis

Due to the existence of current source in the solving region, the finite element analysis can calculate magnetic potential of the node by Ansoft Maxwell software.

According to Maxwell equations, magnetic density B and magnetic field intensity H can be expressed as:

$$B = \nabla \times A \tag{6}$$

$$H = \frac{B}{\mu_r \mu_0} \tag{7}$$

Based on the principle of virtual work in Maxwell, the magneto-static torque can be represented as:

$$T_B = \frac{dW}{d\theta} \Big|_{i=\text{const}} = \frac{\partial}{\partial \theta} \left[\int_V \left(\int_0^H B \cdot dH \right) dV \right] \tag{8}$$

where W is the magnetic co-energy, θ the rotor angle, and i the constant current.

Similarly, based on the principle of virtual work in Maxwell, magneto-static force can be calculated as:

$$F = \frac{dW}{dx} \Big|_{i=\text{const}} = \frac{\partial}{\partial x} \left[\int_V \left(\int_0^H B \bullet dH \right) dV \right] \tag{9}$$

4.2. Characteristics of Magnetic Field

Figure 9 shows the biased magnetic density distribution of the PM in HEDSBSRM and the magnetic density on the circumference of air gap 2. It can be seen that the biased magnetic flux generated by the PM is symmetrically distributed. The magnetic density of area 1 is equal to that of area 2 in Fig.9(a), which means $F_x = 0$ N under this situation. The magnetic density of air gap 2 in the suspension system is about 0.65 T.

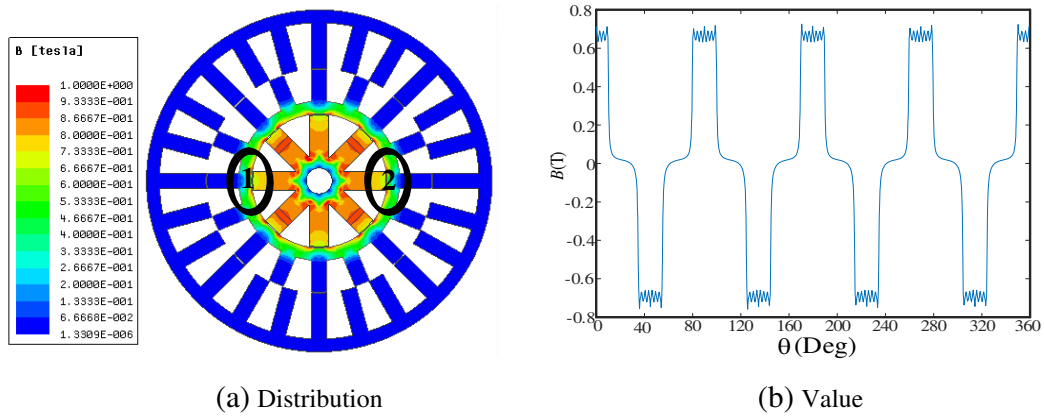


Figure 9. Biased magnetic density of PM.

When $i_x = 2$ A and $i_A = 4$ A, the magnetic flux and magnetic density distribution of the motor are shown in Fig. 10. The torque and suspension magnetic field are independent. The torque magnetic field is symmetrical and evenly distributed in 8 poles. As shown in Fig. 10(b), the magnetic density in area 1 is larger than area 2, which generates a suspension force in the negative x -direction.

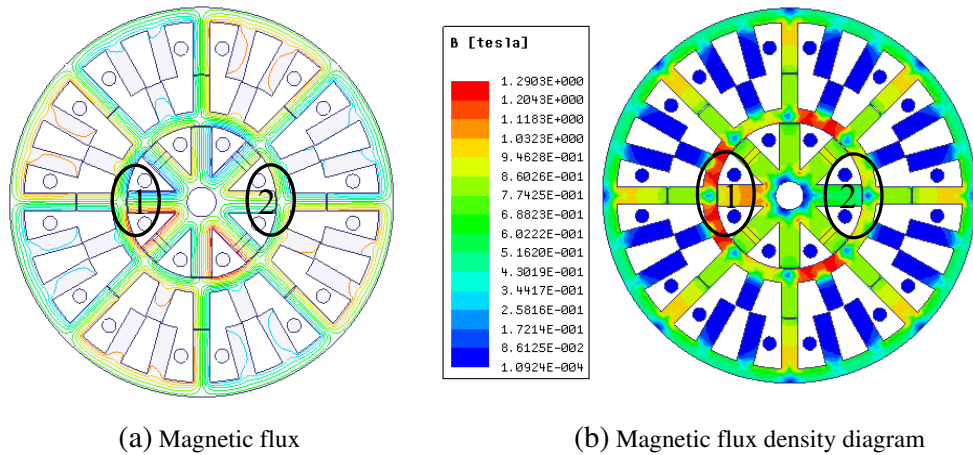


Figure 10. Distribution of magnetic field.

4.3. Characteristics of Torque

When $i_A = 1\text{ A} \sim 4\text{ A}$, the relationship between the torque T and rotation angle θ is shown in Fig. 11. When the rotor is at the aligned position, T is basically zero, and T increases with the enlargement of i_A .

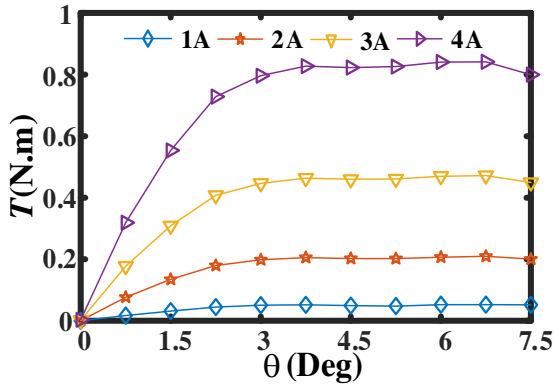


Figure 11. Value of torque.

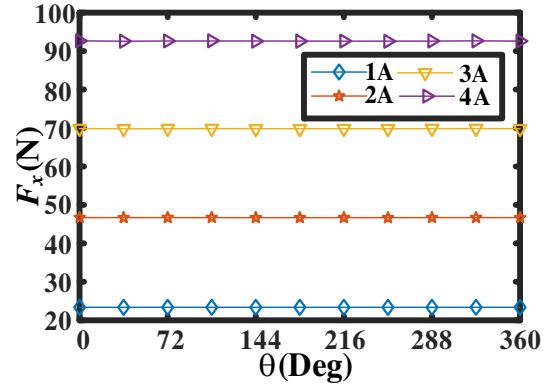


Figure 12. Value of F_x .

4.4. Characteristics of Suspension

When $i_x = 1\text{ A} \sim 4\text{ A}$, the relationship between the generated F_x and θ is shown in Fig. 12. It can be seen that F_x does not change with θ . It remains basically constant. The effective suspension force is still provided in the critical alignment position. This improves the suspension loading capacity in the whole cycle of the motor operation. In addition, as i_x increases, F_x increases.

4.5. Characteristics of Coupling

When $i_A = 4\text{ A}$, $i_x = 0\text{ A}$ and $i_A = 0\text{ A}$, $i_x = 2\text{ A}$, the magnetic flux is as shown in Fig. 13. The magnetic field of torque is generated only through the rotor and outer-stator. The magnetic field of suspension is generated only through the rotor and inner-stator. The excitation of i_A and i_x has no effect on the magnetic field of the other part, which means that T and F_x are not coupled. The decoupling characteristics are initially verified.

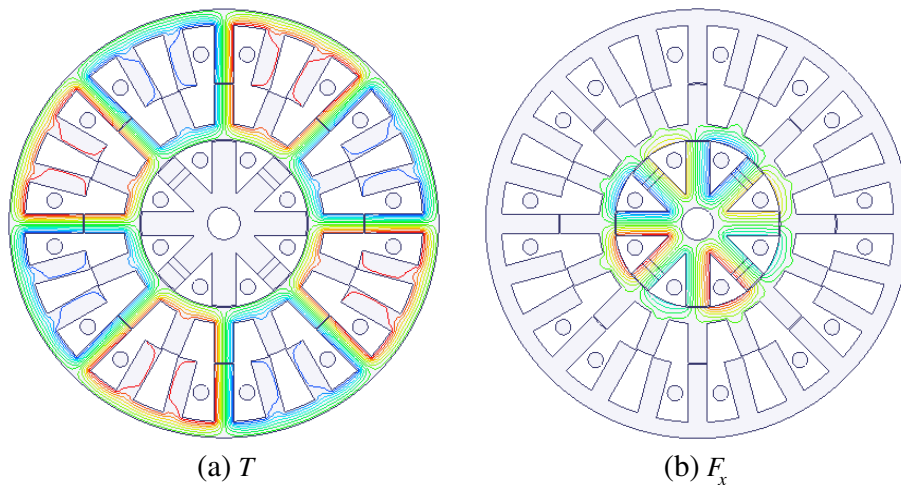


Figure 13. Distribution of magnetic field.

Figure 14 shows the self-inductance of i_A and i_x and the mutual inductance when they are energized at the same time. Compared to the self-inductance, the mutual inductance is almost zero. The coupling between them is small, which verifies the decoupling characteristics again.

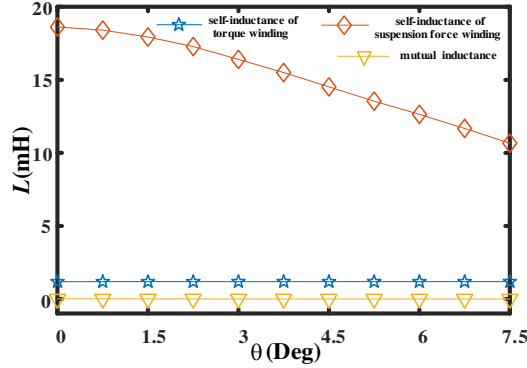


Figure 14. Self and mutual inductance.

Figure 15 shows the coupling between T and F_x when $\theta = 7.5^\circ$. Fig. 15(a) shows the effect of i_A on F_x when i_A and i_x are simultaneously energized. When i_A and i_x increase linearly at the same time, F_x increases with the increase of i_x . Thus, i_A has less impact on F_x . Fig. 15(b) shows the effect of i_x on T . T increases as i_A increases while i_x has less effect on T .

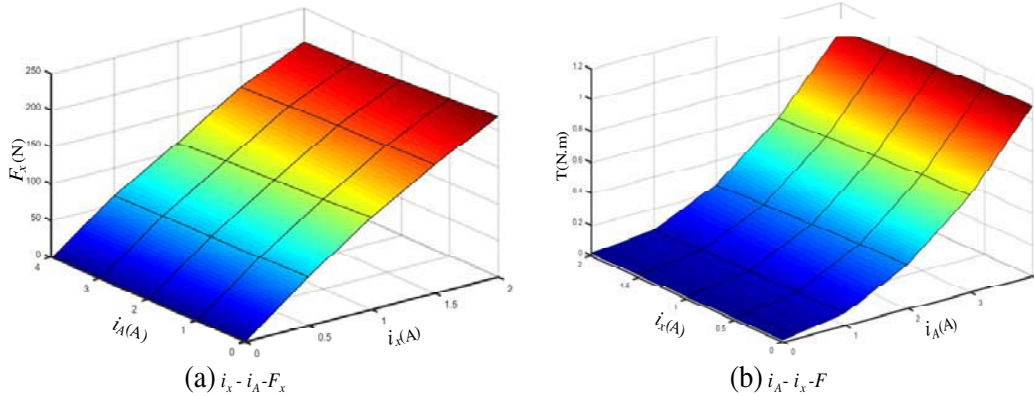


Figure 15. Coupling between T and F_x .

Figure 16 shows the coupling between F_x and F_y when $\theta = 7.5^\circ$. When i_x and i_y are powered on at the same time, their respective effects on the suspension force of the other party are shown in the figure. As shown in Fig. 16(a), when i_x and i_y increase simultaneously, F_x is only related to i_x and has nothing to do with i_y . In Fig. 16(b), F_y is only related to i_y .

From the analysis of Figs. 15 and 16, it can be concluded that not only the coupling between T and F_x is small, but also the coupling between i_x and i_y is small. There is no mutual influence between them, which is conducive to precise control.

For the motor, the decoupling characteristics between T and F_x and between F_x and F_y are verified from the above three aspects. It is beneficial to the subsequent motor control.

4.6. Comparison of Characteristic

The comparisons of characteristic with DSBSRM at the same current and volume are shown in Fig. 17. For the DSBSRM, since the size of inner-stator is small, and it is excited by an electric excitation method,

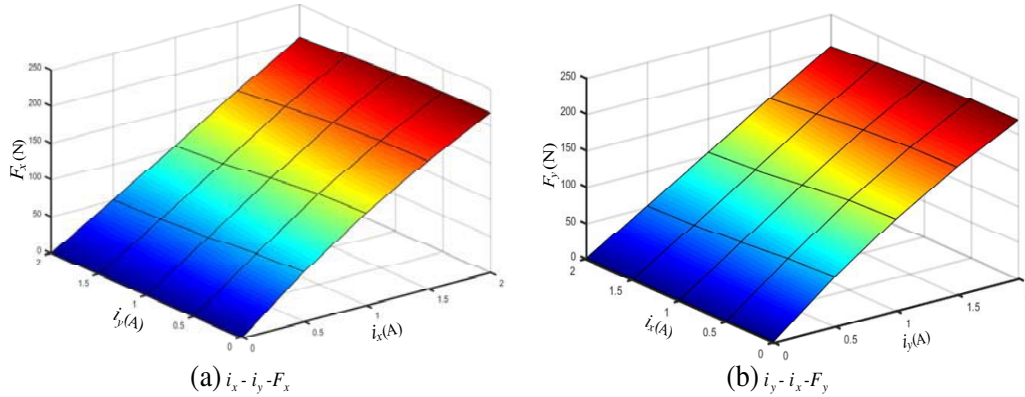


Figure 16. Coupling between F_x and F_y .

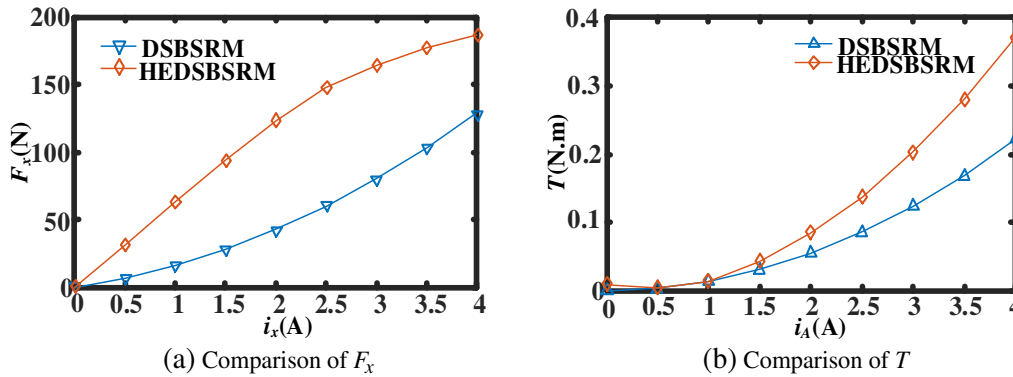


Figure 17. Comparison of characteristic with DSBSRM.

the suspension force is limited, and the power is small. Therefore, permanent magnets are added to the inner-stator to increase the suspension force. In Fig. 17(a), when $i_x = 0 \text{ A} \sim 4 \text{ A}$, suspension force of HEDSERM is greater than that of DSBSRM. In particular, when $i_x = 2.5 \text{ A}$, HEDSBSRM increases nearly 1.5 times. For the HEDSBSRM, due to the phenomenon of magnetic saturation, the rate of change first increases and then decreases. In addition, when their suspension forces are equal, the current required by HEDSBSRM is significantly smaller than DSBSRM. This indicates that HEDSBSRM can reduce power loss and improve radial loading capacity. In Fig. 17(b), when $i_A = 0 \text{ A} \sim 4 \text{ A}$, torque of HEDSERM is greater than that of DSBSRM. It can be seen that the growth rate increases with the gradual increase of current. In particular, when $i_A = 4 \text{ A}$, HEDSBSRM increases nearly 68%.

5. CONCLUSION

In this paper, a novel hybrid excitation double stator bearingless switched reluctance motor is proposed. Compared with traditional double stator bearingless switched reluctance motor, it has the following performance.

- (1) The HEDSBSRM utilizes PM to provide radial biased magnetic flux. Thus, it improves the power and reduces the power consumption.
- (2) Through multi-objective sensitivity analysis and optimization of the key dimensions, performance of the motor is further optimized.
- (3) In addition to decoupling, the suspension force does not change with the rotation angle. Therefore, the suspension loading capacity of the motor operation in the whole cycle is improved. Besides, the problem of insufficient suspension force of the traditional BSRM during commutation is solved.

- (4) The HEDSBSRM achieves decoupling between torque and suspension force. And the two degrees of freedom suspension force can also be decoupled. The electromagnetic characteristic of the proposed HEDSBSRM is better than that of the traditional DSBSRM, and the control is convenient.

ACKNOWLEDGMENT

The project was supported by the Natural Science Foundation of Jiangsu Province (BK 20150510) and Senior Talent Research Funding of Jiangsu University (14JDG075).

REFERENCES

1. Morrison, C. R., M. W. Siebert, and E. J. Ho, "Electromagnetic forces in a hybrid magnetic-bearing switched-reluctance motor," *IEEE Trans. Magn.*, Vol. 44, No. 12, 4626–4638, Dec. 2008.
2. Sun, X., Y. Chen, S. Wang, G. Lei, Z. Yang, and S. Han, "Core losses analysis of a novel 16/10 segmented rotor switched reluctance BSG motor for HEVs using nonlinear lumped parameter equivalent circuit model," *IEEE/ASME Trans. Mech.*, Vol. 23, No. 2, 747–757, Feb. 2018.
3. Xue, X. D., K. W. E. Cheng, T. W. Ng, and N. C. Cheung, "Multi-objective optimization design of in-wheel switched reluctance motors in electric vehicles," *IEEE Trans. Ind. Electron.*, Vol. 57, No. 9, 2980–2987, Sep. 2010.
4. Torkaman, H., E. Afjei, and M. S. Toulabi, "New double-layer-per-phase isolated switched reluctance motor: Concept, numerical analysis, and experimental confirmation," *IEEE Trans. Ind. Electron.*, Vol. 59, No. 2, 830–838, Feb. 2012.
5. Sun, X., L. Chen, H. Jiang, Z. Yang, J. Chen, and W. Zhang, "High-performance control for a bearingless permanent-magnet synchronous motor using neural network inverse scheme plus internal model controllers," *IEEE Trans. Ind. Electron.*, Vol. 63, No. 6, 3479–3488, Jun. 2016.
6. Asama, J., Y. Hamasaki, T. Oiwa, and A. Chiba, "Proposal and analysis of a novel single-drive bearingless motor," *IEEE Trans. Ind. Electron.*, Vol. 60, No. 1, 129–138, Jan. 2013.
7. Sun, X., Z. Shi, L. Chen, and Z. Yang, "Internal model control for a bearingless permanent magnet synchronous motor based on inverse system method" *IEEE Trans. Energy Convers.*, Vol. 31, No. 4, 1539–1548, Dec. 2016.
8. Matsuzaki, T., M. Takemoto, S. Ogasawara, S. Ota, K. Oi, and D. Matsushashi, "Operational characteristics of an IPM-type bearingless motor with 2-pole motor windings and 4-pole suspension windings," *IEEE Trans. Ind. Appl.*, Vol. 53, No. 6, 5383–5392, Nov.–Dec. 2017.
9. Sun, X., L. Chen, and Z. Yang, "Overview of bearingless permanent-magnet synchronous motors," *IEEE Trans. Ind. Electron.*, Vol. 60, No. 12, 5528–5538, Dec. 2013.
10. Sun, X., L. Chen, Z. Yang, and H. Zhu, "Speed-sensorless vector control of a bearingless induction motor with artificial neural network inverse speed observer," *IEEE/ASME Trans. Mech.*, Vol. 18, No. 4, 1357–1366, Aug. 2013.
11. Cao, X., J. Zhou, C. Liu, and Z. Deng, "Advanced control method for single-winding bearingless switched reluctance motor to reduce torque ripple and radial displacement," *IEEE Trans. Energy Convers.*, Vol. 32, No. 4, 1533–1543, Dec. 2017.
12. Wang, H., J. Bao, B. Xue, and J. Liu, "Control of suspending force in novel permanent-magnet-biased bearingless switched reluctance motor," *IEEE Trans. Ind. Electron.*, Vol. 62, No. 7, 4298–4306, Jul. 2015.
13. Cao, X., Z. Deng, G. Yang, and X. Wang, "Independent control of average torque and radial force in bearingless switched-reluctance motors with hybrid excitations," *IEEE Trans. Power Electron.*, Vol. 24, No. 5, 1376–1385, Jul. 2009.
14. Liu, J., H. Wang, J. Bao, G. Zhou, and F. Zhang, "A novel permanent magnet biased bearingless switched reluctance motor," *IEEE Trans. Ind. Electron.*, Vol. 61, No. 12, 4342–4347, Sep. 2013.
15. Wang, H., J. Liu, J. Bao, and B. Xue, "A Novel bearingless switched reluctance motor with a biased permanent magnet," *IEEE Trans. Ind. Electron.*, Vol. 61, No. 12, 6947–6955, Dec. 2014.

16. Xue, B., H. Wang, and J. Bao, "Design of novel 12/14 bearingless permanent biased switched reluctance motor," *IEEE International Conference on Electrical Machines and Systems.*, 2655–2660, Oct. 2014.
17. Wei, P., D. Lee, and J. Ahn, "Design and analysis of double stator type bearingless switched reluctance motor," *Transactions of the Korean Institute of Electrical Engineers*, Vol. 60, No. 4, 746–752, 2011.
18. Zhang, J., H. Wang, L. Chen, C. Tan, and Y. Wang, "Multi-objective optimal design of bearingless switched reluctance motor based on multi-objective genetic particle swarm optimizer," *IEEE Trans. Magn.*, Vol. 54, No. 1, 113, Oct. 2017.
19. Chen, L. and W. Hofmann, "Speed regulation technique of one bearingless 8/6 switched reluctance motor with simpler single winding structure," *IEEE Trans. Ind. Electron.*, Vol. 59, No. 6, 2592–2600, Jun. 2012.
20. Cao, X. and Z. Deng, "A full-period generating mode for bearingless switched reluctance generators," *IEEE Transactions on Applied Superconductivity*, Vol. 20, No. 3, 1072–1076, Mar. 2010.
21. Liu, J., X. Zhang, H. Wang, and J. Bao, "Iron loss characteristic for the novel bearingless switched reluctance motor," *IEEE*, 586–592, Oct. 2013.